Mechanical characterization of regenerating *Hydra* tissue spheres

Mechanics of regenerating *Hydra*

Thomas Perros[1], Anaïs Biquet-Bisquert[1,2], Zacchari Ben Meriem[3], Morgan Delarue[3], Pierre Joseph[3], Philippe Marcq[4], Olivier Cochet-Escartin[1,*]

1 : Institute for Light and Matter, UMR5306, Université Lyon 1-CNRS, Université de Lyon, Villeurbanne, France

2 : Centre de Biologie Structurale, Université de Montpellier-CNRS-INSERM, Montpellier, France.

3 : Laboratory for Analysis and Architecture of Systems, Université de Toulouse-CNRS, UPS, INP, Toulouse, France.

4 : Physique et Mécanique des Milieux Hétérogènes, PMMH, CNRS, ESPCI Paris, Université PSL, Sorbonne Université, Université Paris Cité, F-75005, Paris, France

* : correspondence should be addressed to olivier.cochet-escartin@univ-lyon1.fr

Abstract

Hydra vulgaris, long known for its remarkable regenerative capabilities, is also a longstanding source of inspiration for models of spontaneous patterning. Recently, it became clear that early patterning during Hydra regeneration is an integrated mechano-chemical process where morphogen dynamics is influenced by tissue mechanics. One roadblock to understand Hydra self-organization is our lack of knowledge about the mechanical properties of these organisms. In this paper, we combined microfluidic developments to perform parallelized microaspiration rheological experiments and numerical simulations to characterize these mechanical properties. We found three different behaviors depending on the applied stresses: an elastic response, a visco-elastic one and tissue rupture. Using models of deformable shells, we quantify their Young's modulus, shear viscosity as well as the critical stresses required to switch between behaviors. Based on these experimental results, we propose a description of the tissue mechanics during normal regeneration. Our results provide a first step towards the development of original mechano-chemical models of patterning grounded in quantitative, experimental data.

Statement of significance

Hydra vulgaris is a remarkable organism thanks to its regenerative abilities. One can cut this animal into several pieces which will reform a full *Hydra* in a few days. In this process, the pieces have to define a new organizing axis. Recently, researchers have shown that this axis definition is under mechanical control. One roadblock to understand the relationship between tissue mechanics and *Hydra* biology is our lack of knowledge about the mechanical state of this organism. Here, we perform a mechanical characterization using a combination of microaspiration setups and numerical simulations. We finally propose a description of what happens at the mechanical level during *Hydra* regeneration, allowing quantitative approaches questioning the role of mechanical cues in axis definition.

Introduction

Hydra vulgaris has long been a model of choice in developmental biology because of its remarkable regenerative capabilities (1,2). Almost any excised tissue piece as well as cellular re-aggregates are capable of reforming a fully viable adult in just a few days. In the former example, an excised tissue piece folds back into a closed spherical shape with both its epithelial monolayers, endoderm and ectoderm, engulfing a water-filled lumen. In the latter, the same tissues start by spontaneously sorting into their relative positions (3,4) before expelling excess cells to reform a hollow sphere. At this point, both regenerative trajectories converge and these tissue spheres start undergoing osmotically-driven oscillations during which they swell because of water flowing from the environment to the lumen up to the point where the tension building up within the tissues becomes too large and leads to a local rupture (5,6). After rupture, the samples deflate, close the resulting wound and start another swelling-rupture cycle. These osmotic oscillations induce deformations and therefore stresses within the tissues with relative changes in the radii of the spheres up to 30%. These have been referred to as phase I oscillations and are characterized by a high amplitude and a low frequency. Indeed, after a few of these cycles, the oscillations clearly change and enter phase II where they have lower amplitude and higher frequency (6).

In parallel to these mechanical oscillations, the samples establish a chemical pattern involving some characterized morphogens to define the oral-aboral axis of the organism. Most notably, a local expression of HyWnt3 has been shown to be an early signal of axial patterning with this activation defining the future position of the head organizer (7). This local activation is then followed by the establishment of various chemical gradients within the spheres effectively patterning the whole axis (8,9). At that point, the originally symmetrical samples start elongating in an oblong shape at which ends the adult organs of the head and foot will be regenerated, and the patterning can be considered complete. The switch between phase I and phase II oscillations was thought to be a signature of the establishment of axial patterning (6,10). Since small excised tissue pieces showed both phases, it was thought that they underwent spontaneous symmetry breaking and retained no memory of axial patterning just as cellular re-aggregates.

The question was then to determine how the spherical symmetry was broken during phase I oscillations and how the local head organizer was defined. For a long time, the main hypothesis was that of a purely biochemical spontaneous symmetry breaking in the form of Turing-instabilities of an unknown reaction-diffusion system. In his seminal work, partially inspired by *Hydra* regeneration, Turing has shown how a system of two interacting and diffusing chemical species, which he named morphogens, could become unstable in their homogenous state and spontaneously start forming structures such as dots or stripes (11). These ideas were critical in developing the field of pattern formation and have been adapted to a wide variety of systems and organisms (see for example (12,13) for recent reviews in the context of developmental biology). In this historical development, *Hydra* has retained its place as a model organism. Notably, Gierer and Meinhardt have expanded on the seminal ideas of Turing and developed a modified version of his reaction-diffusion system specifically designed to explain regeneration and grafting experiments in *Hydra* (14). As a result, the so-called Gierer-Meinhardt model has long been the gold standard in the field. At its inception, it was purely speculative but, since then, some proteins have been shown to possess many of the characteristics required by the Gierer-Meinhardt model. Most notably, the protein HyWnt3, involved in the canonical Wnt pathway is now generally considered to be the activator represented in the Gierer-Meinhardt model (15) since its expression is restricted to the head organizer, it has self-activating capacities and it is the first temporal signature of symmetry breaking during regeneration.

Still, these models ignore the mechanical aspects of the process, most notably the osmotic oscillations although it is now well established that they are necessary for proper regeneration (16,17). This observation suggested a possible coupling between the mechanical state of the tissues and their biological response, as has been observed in a variety of contexts and organisms with impacts on cell division or gene expression including in the canonical Wnt pathway (18–21). Recent results have demonstrated such a coupling in *Hydra* by which the expression of HyWnt3 is reduced when osmotic oscillations are blocked (17) providing a potential direct coupling between tissue mechanics and chemical patterning.

Recent modelling efforts have thus been made in order to incorporate mechano-chemical couplings (16,22,23), for instance by making the diffusion constant of the morphogens within the tissues dependent on tissue stretch (16). In most cases though, these couplings were not grounded in experimental evidence. In addition, recent experimental results have started to question the assumptions described so far and underlying these models. First, it was shown that the shift from phase I to phase II oscillations was not a direct signature of axial patterning being established. Instead, the onset of phase II is due to the early apparition of the *Hydra* mouth (24) allowing it to regulate its osmotic imbalance by mouth opening rather than by tissue rupture. One consequence was that axial patterning had to be anterior to the shift between oscillation phases. It then became unclear whether

small excised tissue pieces really went through *de novo* patterning or if they could inherit this patterning from their original host organism. Recent experimental results show that they do retain axial patterning although the exact mechanism by which they do so remains unclear, whether by the organization of their ectodermal actin structures called myonemes (25) or by pre-existing biochemical gradients (26).

Although small excised tissue pieces retain axial patterning, it still remains that 1- cellular re-aggregates which cannot conserve either supracellular actin structures or chemical gradients have to show *de novo* axial patterning during osmotic oscillations, 2- there is evidence of a direct coupling between tissue deformations and Hywnt3 expression (17), one of the most important morphogens involved in *Hydra* patterning and 3- osmotic oscillations are required for the proper elongation, morphogenesis and regeneration of both excised tissue pieces and cellular re-aggregates. For all these reasons, the focus of the field is currently shifting to an integrated view of *Hydra* regeneration as a mechano-biological process (23,27). One clear roadblock to the development of these ideas is our lack of understanding of the rheological properties and mechanical state of regenerating *Hydra* tissue spheres. This often leads to assumptions as to the rheology of these samples and rough estimates of their key mechanical parameters. One exception is the development by Veschgini and colleagues of a two-fingered robotic hand allowing them to apply known, constant deformations on the tissue spheres and measure the resulting forces (28) giving the first local, quantitative measurements of mechanical features in *Hydra*. These measurements were not, however, used to deepen our understanding of the spontaneous osmotic oscillations.

In this work, we try to overcome these limitations and to offer a quantitative characterization of the mechanics of *Hydra* tissue spheres. To do so, we used the well-established micro-aspiration technique (29–32) which we adapted to increase its throughput through the use of original microfluidic constructs following (33). We found three different mechanical behaviors as the aspiration pressure was increased: first an elastic response, then a viscoelastic one and finally tissue rupture, as observed in phase I oscillations. Combining our experimental observations and measurements with the development of a rheological model of elastic shells and numerical simulations, we obtained quantitative measurements of both the main rheological parameters of *Hydra* tissue spheres and the critical pressures required to switch between the three regimes. Thanks to these results, we provide a description of internal tissue mechanics, strains and stresses during osmotic oscillations. Hopefully, this mechanical characterization will serve as a stepping stone for the study of mechano-biochemical couplings in a quantitative manner.

Material and Methods

Hydra maintenance and lines used

3 *Hydra vulgaris* lines were maintained and used for experiments: a watermelon (WM) line (ectoderm GFP / endoderm DsRed2), a reverse watermelon (RWM) one (ectoderm DsRed2 / endoderm GFP) and the AEP line from which embryos were obtained for making transgenic animals. Hydras were kept in *Hydra* medium (HM), which consists of 1mM $CaCl_2$, 0.1mM $MgCl_2$, 0.3mM KNO_3, 0.5mM $NaHCO_3$ and 0.08mM $MgSO_4$ at a PH between 7 and 7.3. Cultures were stored at 18°C in the dark in an incubator (Pol-Ekko-Aparatura). Animals were fed two to three times per week with newly hatched Artemia (Hobby) and cleaned every two days by changing the medium in which they sit. Animals were starved for at least 24h before the start of any experiment.

Preparation of tissue spheres

Tissue spheres were made by cutting a whole animal using a sterile scalpel (Holtex, Bistouri UU n°10), as follows: The head and tail were removed by two transverse cuts and the remaining body column was first sliced into 3 or 4 pieces. These pieces were cut further to obtain 6 to 8 samples per adult animal. These samples were left to fold into tissue spheres for 3 to 4 hours in HM.

Design and fabrication of the removable inserts

Sliding elements containing the cylindrical pipettes were fabricated in dry film according to the protocol detailed in (33). Briefly, photolithography was realized on a 500 µm-thick photosensitive dry film (DF series), laminated on a silicon wafer. Lateral dimension of the photolithography mask defined the length of the insert (20 mm) and its height (1 mm), as well as pipette diameter (50 and 100 µm were used). 100 µm-wide square openings placed at the bottom of the insert were also used for imaging purposes in Movie S2. After post-exposure bake on a hot-plate, the inserts were released from the wafer during overnight development in an acetone bath that both revealed the patterns and unstick the dry films from the wafer. A single fabrication run allowed to fabricate 100 such sliding elements

Mounting and preparing of the microfluidic device

We used a microfluidic tool that allows several micro aspirations to be performed in parallel. This system is composed of a chamber crossed by a removable insert bearing multiple tunnels allowing suction to happen. Both the chambers and inserts were designed using the CAD software Inventor 2020 (Autodesk). The chamber is composed of a main channel which is 20.5mm long, 4mm wide and 0.5mm high (see Fig S1 for the schematics). Halfway through its length, it is barred by another channel which will host the removable insert. The perpendicular channel is 13mm long, 0.5mm wide and 1mm high (Fig S1).

From this design, a mold was manufactured by micromilling using the CNC Mini-Mill/GX (Minitech machinery corporation) with a two size cutter of 1mm diameter on a brass template. The chamber was then made of polydimethylsiloxane (PDMS) (Sylgard 184, Dow Corning) supplemented with 10% curing agent (Dow Corning) from the mold. The PDMS was left to solidify overnight at 70°C and the channel was manually peeled. Inlets and outlets were created by manual punching using a 1mm wide puncher (Harris Uni-Core) at each end of the main channel. The insert channel was opened by manual, transverse cutting to allow insertion of the sliding element. The resulting channel was then bound to a thin PDMS layer, itself bound to a glass slide (Biosigma VBS655/A) by using an oxygen plasma cleaner (Harrick plasma PDC002 with the associated PlasmaFlo gaz mixer). The thin PDMS layer was used to facilitate the introduction of the insert by avoiding direct friction with the glass slide and to avoid leakage. This introduction is done manually with tweezers and is aided by the fact that the insert cannot deviate from its associated channel because of the height difference between both channels. The outlet was connected to a plastic tube of 0.5mm internal diameter and 1.25mm external diameter, sealed at the other end by a 0.6x30mm needle (BD, microlance 3) attached to a 3mL syringe (Braun, Omnifix3P). The needle is deliberately slightly wider than the tube to ensure a hermetic connection. The whole setup was placed in a 100mm Petri dish and immersed in HM. By slowly removing the syringe's plunger, the channel started filling with HM from the inlet all the way to the syringe while avoiding to create air bubbles in the main channel and checking for proper sealing of the system. Once the plunger was fully removed, the height difference ΔH between the water in the syringe and the water in the Petri dish (see Fig S2 for a schematic of the whole setup) was manually controlled and created a pressure difference between chamber inlet and outlet according to:

$$\Delta P = \rho g \Delta H$$

Where ρ is the HM density and g the gravitational acceleration.

Micro-aspiration experiments and data analysis

The syringe was first placed 4cm below the water level of the dish to create a light water flow induced by hydrostatic pressure. Several *Hydra* tissue spheres were manually pipetted into the inlet and were thus naturally driven to the holes in the inserts by the water flow, at which point the height difference was set back to 0 for a couple of minutes. A typical experiment could then be started by the application of a controlled pressure by moving the syringe down again. Images were captured under a microscope (Zeiss Axio Vert.A1 equipped with an Axiocam 202 camera). In most experiments, timelapses were recorded in fluorescent microscopy using WM and RWM lines.

In the case of elastic measurements, increasing steps of pressure were applied onto the same samples. Each step lasted for 10min and images were recorded every 10s to make sure that no flow was observed on the samples. After these 10min, the samples were released for 5min to allow them to regain their original shape before applying a new, larger pressure difference.

For visco-elastic measurements, a single pressure step was applied and samples were imaged by fluorescent microscopy for 30min with a 10s time step and the dynamics of the aspirated length was monitored.

To automate the measurement of the aspirated length in these experiments, kymographs of the aspirated tongue were generated in ImageJ (NIH), binarized and analyzed in Python with custom made code to extract the length of the tongue in each image. For elastic measurements, the average length over the last 5min of recording was used whereas for visco-elastic measurements, the whole dynamics was kept.

The acquired images were also used to measure the mean projected area *A* of each analyzed sample by usual thresholding techniques in ImageJ. This measurement was then turned into an average radius *R* as $R = \sqrt{\frac{A}{\pi}}$.

Osmotic oscillations measurements

To measure osmotic oscillations shown in Fig 6 and Fig S6, *Hydra* tissue spheres were prepared as described above. In parallel, a 1% agarose gel was prepared at the bottom of a Petri dish, left to solidify and was manually punched to create 1mm wide wells which then hosted the samples. These wells were used to limit the samples movement during osmotic oscillations. They were then imaged for 24h at a 15min interval. The resulting images were thresholded and analyzed in ImageJ to extract the projected area as a function of time $A(t)$. Finally, the samples' radii $R(t)$ were computed as described above. The equilibrium radius R_0 of a given sample was defined as the minimum of $R(t)$ over the whole recording allowing us to estimate the strains on the inflating sphere.

Extraction of rheological parameters

To measure Young's moduli in the elastic phase, each sample was treated separately. Based on the acquired images, we measured their projected area $S_0$and turned them into rest radii $R_0 = \sqrt{\frac{S_0}{\pi}}$. Then, we used our measurements of ΔP as a function of δz (Eq 3) and fitted them by a straight line in Python. The slope of this straight line was kept and multiplied, according to Eq 4, by $\frac{(1-\nu)R_0^2}{2C_S Eh}$ to extract the Young's modulus of that specific sample. We then repeated the procedure on n=31 samples and report the mean and standard deviation of this distribution in the text.

In the visco-elastic phase, we measured the dynamics of the aspirated length as a function of time $L(t)$ and fitted them in Python according to Eq 5. To extract Young's moduli, we used the same formula as above except that we replaced the slope of a linear fit of several points by the ratio of ΔP over $\delta(1-\kappa)$, δ and κ stemming from the fit of the full dynamics.

To estimate the order of magnitude of the effective viscosities in the same experiments, we used the same fit according to Eq 5 to extract the speed of tissue flow U and estimated the viscosity as $\eta = \frac{\Delta P R_p}{U C_v}$ with $C_v = 1$.

Finite element simulations

Numerical simulations were performed with the finite-element solver Comsol Multiphysics (COMSOL, Inc). The micropipette was represented as a stiff (Young's modulus $E_p = 10^9 Pa$), nearly incompressible (Poisson's ratio $\nu_p = 0.49$) cylinder of inner radius $R_p = 50\mu m$. The reference state of the *Hydra* sphere was a shell of outer radius $R_0 + {}^{h}/_{2}$ and inner radius $R_0 - {}^{h}/_{2}$, whose center O was located on the cylinder's longitudinal symmetry axis Oz. We denote by E and ν the Young's modulus ($E \approx 10^4 Pa$) and Poisson's ratio ($0.4 \leq \nu \leq 0.49$) of the tissue. The external pressure ΔP was applied on the spherical section contained within the micropipette. Simulations enforced the rotational invariance of the system (*Hydra* + micropipette) about Oz. The equations of linear elasticity were treated within a pressure formulation, adapted to approximately incompressible elastic materials. For each value of the applied pressure, we recorded the maximal deformation observed on the symmetry axis denoted $\delta z(r = 0)$, and computed as a spatial average along the shell's thickness. We checked that our results were robust to smoothing the sharp corner of the micropipette over a scale of the order of $1\mu m$. They were also insensitive to decreasing the typical mesh size.

Measurement and data analysis of threshold pressure measurements.

For the measurement of the pressure thresholds distinguishing each regime, we used the fraction of pieces changing their rheological behavior at different applied pressures. To observe the switch between the elastic and viscous regimes the pressure was gradually increased by lowering the syringe in 3cm increments, starting low enough that no viscoelastic behavior was observed (usually 10 or 14cm). At each pressure level and after 20 minutes, we noted the fraction of pieces that had changed regime and the experiment was stopped when all samples had done so. Kymographs were used to visually separate both regimes. The length profile over time was constant in the elastic regime, whereas it evolved linearly with a clear slope in the viscous regime.

The same strategy was used to measure the rupture threshold but we started at higher applied pressures. Images were taken in transmission, as it facilitated the observation of briefly detached pieces of tissue in the holes of the inserts, the first sign of the rupture regime. They were also taken this time at a rate of ten minutes of suction per threshold. Identifying the switch between the viscous and the rupture regime was done visually.

In both cases, we thus ended up with a fraction of samples adopting a certain behavior as a function of applied pressure. Assuming that individual thresholds are variable and normally distributed, this cumulative frequency followed a sigmoid shape of the form $\frac{1}{1+e^{-(\Delta P-\Delta P_c)/\alpha}}$ where ΔP_c is the threshold pressure at which 50% of samples have switched behavior and α is a parameter controlling the steepness of the sigmoid function. We thus fitted our data with that functional form using Matlab's (Mathworks) curve fitting toolbox. In the manuscript, we report threshold pressures as ΔP_c resulting from the fits and error bars represent the 95% confidence interval of these fits.

EDTA experiments

Rheological measurements on *Hydra* whose cell adhesion had been inhibited were carried out by immersing the tissue spheres in 2 mM EDTA solution. This solution was made from a stock solution of 0.5M diluted in HM. The entire microfluidic system was immersed in the solution, and the *Hydra* pieces were left to bathe in it for around ten minutes before aspiration to give the drug time to take effect before measuring. The rest of the protocol was identical to that of the rheological measurements explained above.

Spinning disk imaging

To estimate the thickness of *Hydra* tissue spheres, several WM samples were imaged underneath an Eclipse Ti2 microscope (Nikon) equipped with a CSU-W1 spinning disk unit (Yokogawa) and an Orca Fusion BT camera (Hamamatsu). Z-stacks were automatically acquired with a step of 1 micron and vertical slices were made using ImageJ (Fig S3). The thickness of six samples were manually measured using the same software and were all found to be in the $15 - 25\mu m$ range.

Results

Multiplexed micro-aspiration setup

In order to define and measure the rheological properties of *Hydra* tissue spheres, we settled on the use of micro-aspiration experiments. These experiments are now well-established, robust and measure rheological properties at length scales and frequencies relevant for the regenerative process. Their main drawback is their intrinsically low throughput. In their original form, micro-aspiration experiments can only probe one sample at a time with a single experiment running for around 1h. We thus started by developing and adapting a microfluidics device making use of removable inserts (33) to parallelize the experiment, in the same spirit as the technique developed in (34) but with circular pipettes which prevent singularities and leakage. This device was composed of two different objects. First, a microfluidic channel was designed to host the samples, it was 3cm in length and 500μm in height (Fig 1A, Fig S1). Halfway through this channel and perpendicular to it sat another channel meant to host the removable insert. This channel was 500μm wide and 1mm high. The whole construct was then manufactured in polydimethylsiloxane (PDMS).

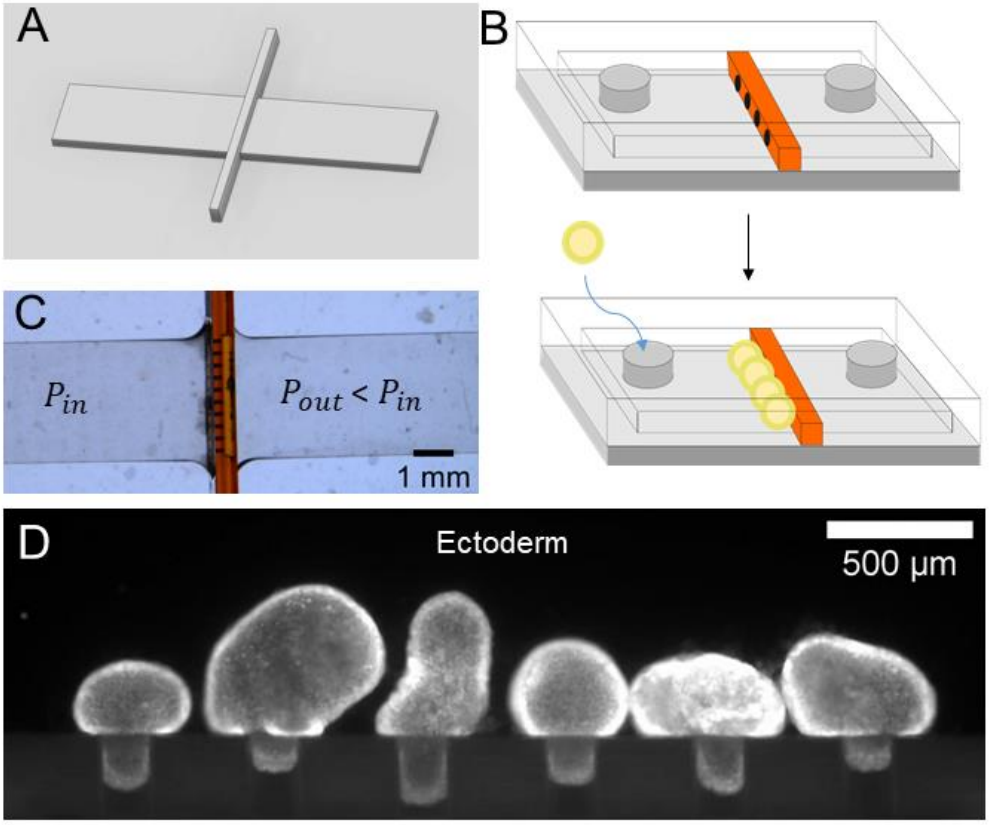

Fig 1. Parallelized micro-aspiration experiments. A: Schematics of the mold for the PDMS channel (details on dimensions can be found in Fig SXX). B: Representation of the principle of the experiment, the insert, in orange, effectively creates an array of cylindrical tunnels, equivalent to model micropipets. The tissue spheres, in yellow, flow towards these openings and, once sealed, get aspirated within. C: Snapshot of a mounted channel with an insert containing ten tunnels in parallel. D: Fluorescent imaging of the ectoderm of six samples aspirated within the tunnels.

These PDMS channels were bound by plasma treatment to a thin PDMS layer which was then bound in the same way to a glass slide. One side of the insert channel was manually cut open to allow insertion while the other end remained closed to ensure hermetic sealing of the whole device after insertion. For the same reason, the insert was designed to be slightly higher and wider than this channel.

The second object was the removable insert made in dry film and patterned by photolithography (see Materials and Methods). As it was manufactured separately, we had full control over the number, position, shape and size of the openings as well as their length which could be smaller than 500µm. Most of the experiments presented here were carried out with removable inserts bearing either 6 or 10 circular openings, 500µm or 300µm away from one another, 300µm in length and 100µm in diameter. Of note, these holes sat, vertically, at the midpoint of the samples' channel (250µm, Fig 1B). Tissue spheres aspirated in these holes therefore didn't touch either the bottom or the top of the PDMS channel which had no influence on the aspiration.

After the manual insertion of the removable insert, both ends of the PDMS channel were punched. The exit side was then connected to a tube leading to a syringe of controllable height. The whole setup was immersed in *Hydra* medium (HM) in a Petri dish (Fig S2). The syringe was then opened by slowly pulling its plunger, filling the whole setup with HM and effectively creating a liquid height difference between the entrance, open in the Petri dish, and the exit, connected to the now open syringe (Fig 1C). This difference in pressure (with $P_{in} > P_{out}$) initially created a flow of water from the Petri dish

346 and the entrance of the device through the holes and into the exit and its syringe. In this step, we could
347 confirm the absence of leaks throughout the setup and therefore airtight sealing.

348 Previously prepared *Hydra* tissue spheres were then manually pipetted into the punched hole on the
349 entrance side. Thanks to the flow of water, the samples naturally aligned with the openings in the
350 insert. Once all openings were blocked by a sample, the flow of water stopped and aspiration of the
351 tissue spheres was observed (Fig 1D, Movie S1). Of note, in most experiments, the height difference
352 was set to 0 as soon as the samples aligned with the holes so that a controlled step in pressure could
353 be applied thereafter.

354 *Rheological behavior depends on applied stress.*

355 Using this multiplexed setup, we started by studying the response of newly formed *Hydra* tissue
356 spheres to micro-aspirations in the kPa range using circular openings with a radius $R_p = 50\mu m$. We
357 observed a seemingly elastic response of the samples in the sense that for a given applied pressure
358 difference, a tongue of tissue was aspirated within the holes which length remained constant after a
359 few tens of seconds. When the pressure was released, we also observed that the samples retrieved
360 their original shape, baring no sign of the aspiration after a few seconds. However, when we increased
361 the applied pressure, we started observing samples flowing inside the holes, a signature of a viscous
362 behavior. When removed from the holes, these samples clearly showed larger deformations which
363 took much longer to retract. Finally, at even higher applied stresses, we started observing rupture of
364 the tissue and cell detachments, reminiscent of the rupture observed under normal phase I osmotic
365 oscillations (Movie S2). Since all three behaviors seemed relevant to understand the mechanical
366 behavior of normally regenerating tissue spheres, we decided to characterize them all, as well as the
367 pressure thresholds between these different phases.

368

369 *Elastic behavior at low applied stresses.*

370 To characterize the elastic behavior of the tissue spheres, we applied steps of pressure on the same
371 samples and recorded, for each step and for each sample in an experiment, the length of the aspirated
372 tongue L (Fig 2A) . We monitored the samples closely to make sure they did not start flowing in the
373 holes, in which case their analysis was stopped. As expected, we found that the higher the pressure,
374 the longer the aspirated tongue (Fig 2A). To estimate a Young's modulus from these measurements,
375 we needed a rheological model of a linearly elastic spherical shell of radius R_0 and thickness h.

376 As is the case for cell aggregates, we expect that intercellular adhesion and cellular cortical tension will
377 contribute to an effective surface tension of the *Hydra* tissue spheres, which we denote by γ.

378 A pressure difference ΔP through the micropipette of radius R_p generates an aspiration force $f_p =$
379 $\pi R_p^2 \Delta P$. For an aspirated length L, the free energy F of the aspirated shell reads:

$$F = 2\gamma S - f_p L \qquad (1)$$

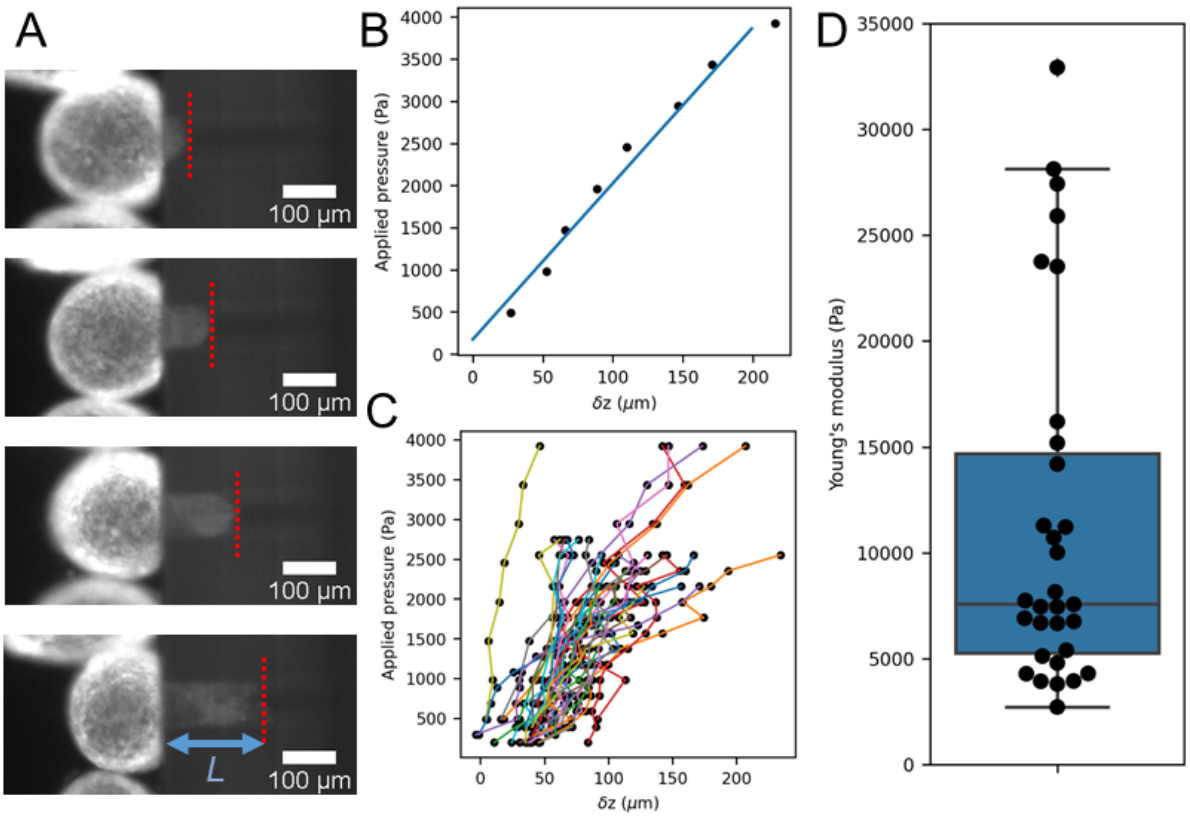

Fig 2. Elastic behavior quantification. A: snapshots of one tissue sphere aspirated in a hole at increasing pressure steps (top to bottom). The dashed red line shows the position of the aspirated tongue at each step and L is the aspirated length. B: Linear relationship between the applied pressure and δz for a single tissue sphere and 8 different pressure steps. C: Same measurement as in B, repeated on n=31 tissue spheres, each represented by a different colored line. D: distribution of Young's moduli obtained by this method. Black dots are individual measurements, the box plot shows the median and quartiles of the distribution. We found E=11.4 ± 8.3 kPa (mean ± standard deviation, n=31).

Where S denotes the surface area of the sample and the factor 2 takes into account the presence of two interfaces. Assuming incompressibility, the volume V of the sample is constant. For small enough deformations during aspiration, we expect that the thickness h of the sample will remain constant. Since $V = Sh$, the surface area of the sample also remains constant $dS = 0$. In other words, in the case of the small deformations of an incompressible shell of approximately constant thickness, tissue surface tension does not contribute to the total force f exerted on the sample:

$$f = -\frac{dF}{dL} = -2\gamma\frac{dS}{dL} + f_p = f_p = \pi R_p^2 \Delta P \qquad (2)$$

Indeed, our experiments do not exhibit a clear half-sphere of radius R_p, typical of the early entry of a full cell aggregate into a micropipette (35). The rest state of the system is thus simply that of the initial spherical shell of radius R_0 and due to that initial curvature the displacement of the tip of the tissue tongue inside the micropipette δz reads:

$$\delta z = L - (R_0 - \sqrt{R_0^2 - R_p^2}) \qquad (3)$$

As expected for an elastic material, we found a linear relationship between this displacement and the applied pressure ΔP (Fig 2B). To make sure that we were not missing a viscous behavior at longer time scales, we tried and managed to trap tissue spheres for tens of hours in this elastic phase without any indication of tissue flow (Movie S3). We also noticed that for many samples, our linear fits had negative intercepts at the origin. This could be the signature of a stress-stiffening effect by which the effective Young's modulus would increase with the applied pressure, *i.e.* the existence of non-linear elastic behavior , as observed in suspended cell monolayers (36). The space and time resolution of these micro-aspiration experiments didn't allow to obtain a definitive explanation but this effect remained small, especially in the context of real osmotic oscillations during regeneration.

In analogy with the elastic behavior of elastic thin spherical shells (see for instance (37)), we expect that the displacement and the applied pressure should be related according to:

$$\Delta P = C_s \frac{2Eh}{(1-\nu)R_0^2}\delta z \qquad (4)$$

Where E and ν are, respectively, the Young's modulus and the Poisson's ratio of the sample and C_s is a dimensionless, geometry-dependent pre-factor. Of note, in this description, we ignore the complex composite structure of the shell which includes two different epithelial layer as well as the extra-cellular matrix.

In order to estimate C_s, we performed numerical simulations of micro-aspiration of elastic spherical shells by a single cylindrical tunnel (Fig 3A). In our experimental data, we had $R_0 = 168 \pm 28\mu m$ (mean ± standard deviation, n=31). We estimated h by spinning disk confocal microscopy (Fig S3) and found it to be on the order of $h = 20 \pm 5\mu m$. As we had no measurement of the Poisson's ratio of our samples, we made an assumption of near incompressibility and set $\nu = 0.49$. Assuming that $C_s = 1$, the order of magnitude of the obtained Young's moduli would be of $10kPa$, we thus set $E = 10kPa$ in these simulations. Based on these values, we submitted spherical shells to applied pressure values ranging from 200Pa to 3000Pa and measured the resulting δz. These simulations confirmed the linear relationship between ΔP and δz (Fig 3B) and allowed to estimate C_s thanks to the knowledge of the value of E. Applying this method, we found $C_s = 1.2$ and used this value in our experimental measurements.

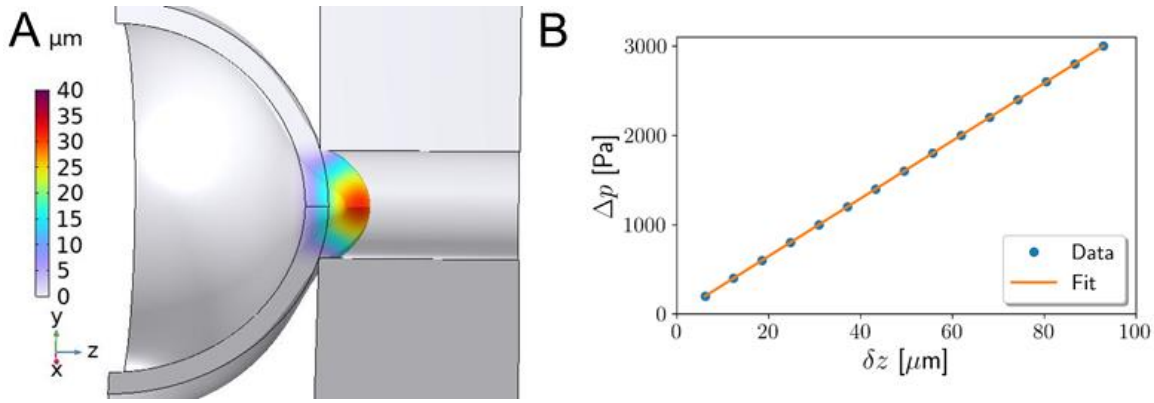

Fig 3. Numerical simulations. A: Graphical representation of the deformed shell under $\Delta p = 10^3\,Pa$. The color code represents the z-component of the displacement field. Black lines delineate the reference state of the system. Parameter values for these simulations are $R_0 = 170\ \mu m$, $h = 20\ \mu m$, $E = 10^4\ Pa$, $\nu = 0.49$. B: applied pressure Δp versus the displacement δz. The slope of the fitted line, in orange, corresponds to a value $C_S = 1.2$.

Thanks to our multiplexed setup, we were able to measure up to six samples in parallel in one sitting. By then repeating these experiments six different times, we achieved a total of 31 tissue spheres (Fig 2C) characterized in that phase. For each of them, we extracted the slope of the linear relationship between ΔP and δz, its initial radius R_0 and finally obtained a quantitative measurement of its Young's modulus using Eq 4 (Fig 2D). Overall, we found the Young's modulus of *Hydra* tissue spheres to be 11.4 ± 8.3 kPa (mean ± standard deviation, n=31). As may be apparent in Fig1, assimilating the geometry of aspirated *Hydras* as a sphere is an approximation which may contribute to the large uncertainty characterizing our estimate of their Young's modulus.

Of note, other element-based numerical simulations were performed with parameters varying in the following ranges: $200 \leq \Delta P \leq 3000Pa$, $0.4 \leq \nu \leq 0.49$,$15 \leq h \leq 25\mu m$,$140 \leq R_0 \leq 200\mu m$, $0.5\ 10^4 \leq E \leq 1.5\ 10^4\ Pa$. In all cases, we found a coefficient C_s of order 1: $0.8 \leq C_s \leq 1.4$ suggesting that the order of magnitude of our results was unaffected by uncertainties on these different parameters (see as well Fig S4).

Visco-elastic behavior at intermediate applied stresses

We then turned our attention to the next observed behavior which involved flowing of the samples within the tunnels. This visco-elastic behavior has long been observed and studied, both on single cells (29,38,39) and multi-cellular spheroids (4,30,35). We followed the usual approach in that situation where a single, controlled pressure step was applied in the device at t=0 after the samples were already placed close to the entrance of the tunnels. The dynamics of the aspirated length $L(t)$ was then recorded by fluorescent microscopy for tens of minutes (Fig 4A). It was important to keep recording on these longer time scales in order to be certain of the behavior adopted by each sample as a very slow flow could easily be discarded as an elastic response if the observation time scale was too short.

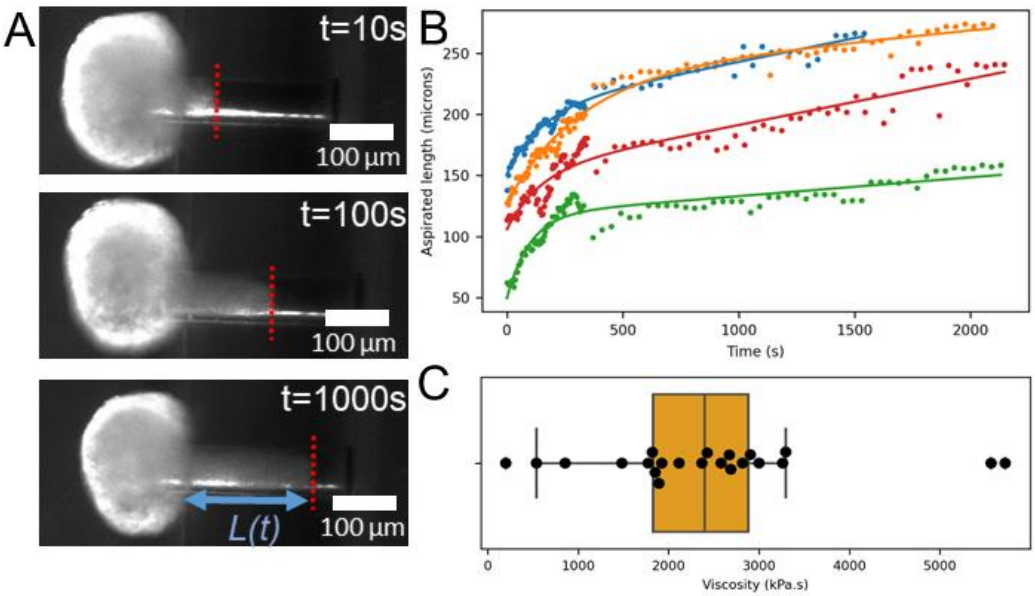

Fig 4. Visco-elastic flow at large applied pressure. A: snapshots of a tissue sphere showing flow at a constant applied pressure. B: four examples of typical dynamics of the flow as a function of time. Dots of different colours represent four independent samples and solid lines fits by Eq 5. C: distribution of measured viscosities as black dots with box-whisker plot in orange. We found it to be (2.4 ± 1.2).10⁶ Pa.s (mean ± standard deviation, n=22).

Since the behavior is qualitatively similar to that observed for cellular aggregates aspirated in cylindrical micropipets, we first applied the well-known modified Maxwell model developed in (30). Briefly, a dashpot representing tissue scale viscosity is combined in series with a standard linear solid

unit incorporating cell scale viscoelasticity as well as tissue scale elasticity. We fitted our data with the form of $L(t)$ predicted by this model:

$$L(t) = \delta\left(1 - \kappa e^{\frac{-t}{\tau}}\right) + Ut \qquad (5)$$

Where δ is linked to the short-term elastic deformation, κ is a constant linked to the relative contributions of the two springs in the standard linear solid unit, τ is the cell scale visco-elastic relaxation-time and U is the long term viscous flow rate. We found that this functional form was also relevant to describe our data quantitatively (Fig 4B) despite the morphological differences between our samples (empty shells) and ball-shaped aggregates (full spheres). We could however employ a scaling argument similar to the one applied in this model to estimate an order of magnitude of the effective viscosity of our samples. As for cellular aggregates, friction between the tissue and the tunnels walls can be neglected since the long-term aspirated length scales not as the square-root of time, but as a linear function of time. Assuming that dissipation is due to cell rearrangements at the entrance of the tunnels thus acting on a length scale of order R_p. The total dissipative force can therefore be approximated as $f_{viscous} \approx C_v R_p U \eta$ with η the viscosity of the samples and C_v a dimensionless, geometrical pre-factor equal to 3π for a ball-shaped aggregate and unknown in our geometry. This viscous force has to be balanced by the aspiration force which we have shown to be $f_p = \pi R_p^2 \Delta P$ which leads to:

$$\eta \approx \frac{\Delta P R_p}{U C_v} \qquad (6)$$

To the best of our knowledge the computation of C_v has never been done for spherical viscous shells and in the same geometry as the one in our experiments. We will see below that a precise measurement of this effective viscosity has little impact on the description of *Hydra* osmotic oscillations and we limited ourselves to obtaining an order of magnitude estimation of the viscosity by taking $C_v = 1$. Note that assuming that tissue scale dissipation acts across the thickness h of this multilayered tissue does not change our estimate as h and R_p have the same order of magnitude. Again, our microaspiration setup allowed us to efficiently gather data on multiple samples and combining them, we found an estimation of the viscosity of (2.4 ± 1.2).10^6 Pa.s (mean ± standard deviation, n=22, Fig 4C).

The full dynamics of aspiration in that phase can also yield measurements of the Young's modulus of the samples. In line with our analysis of the purely elastic response, we expect here that:

$$\Delta P = C_s \frac{2Eh}{(1-\nu)R_0^2}\delta(1-\kappa) \qquad (7)$$

Similar to Eq. 4 with $\delta(1-\kappa)$ the immediate elastic aspirated length in the notation of this model. Applying this relationship to the results of our fitted data, we found again E be in the tens of kPa, in accordance with our results on the purely elastic behavior of *Hydra* tissue spheres.

These visco-elastic experiments were made difficult by the fact that in many instances, we observed, in addition to the flow of the samples, cells detaching at the tip of the aspirated tongue, indicative that the tissues were already rupturing. These cases were obviously discarded from the analysis, limiting

the amount of available data. Overall, it appeared that at these applied pressures, the visco-elastic phase and rupture were often occurring together.

Critical pressures between different behaviors

To further study this question, we then turned our attention to the critical pressures required to transition between the three regimes: elastic, viscoelastic and rupture. We often found cases where, for a given applied pressure, a fraction of the samples loaded in the same setup would behave as elastic solids while other behaved as viscoelastic fluids (Fig 5A). To characterize the first critical pressure, we therefore measured, at different applied pressures, the fraction of samples showing a viscoelastic versus elastic behavior while discarding rupturing ones. We found this fraction to follow a sigmoid shape as a function of the applied pressure and used this function to fit our data (Fig 5B). We defined the critical pressure as the center of this sigmoid where 50% of samples had switched from one behavior to the other. Following this method, we found the critical pressure between elastic and viscoelastic behaviors to be 2.22 ± 0.14 kPa (error bars represent the 95% confidence interval of the sigmoid fit). We then employed the same strategy to characterize the critical pressure leading to tissue rupture (Fig 5C). We found it to be 2.37 +- 0.08 kPa, very close to the previous one confirming our intuition that both behaviors were linked together and that tissue flows inside the holes were already a signature of their lack of integrity.

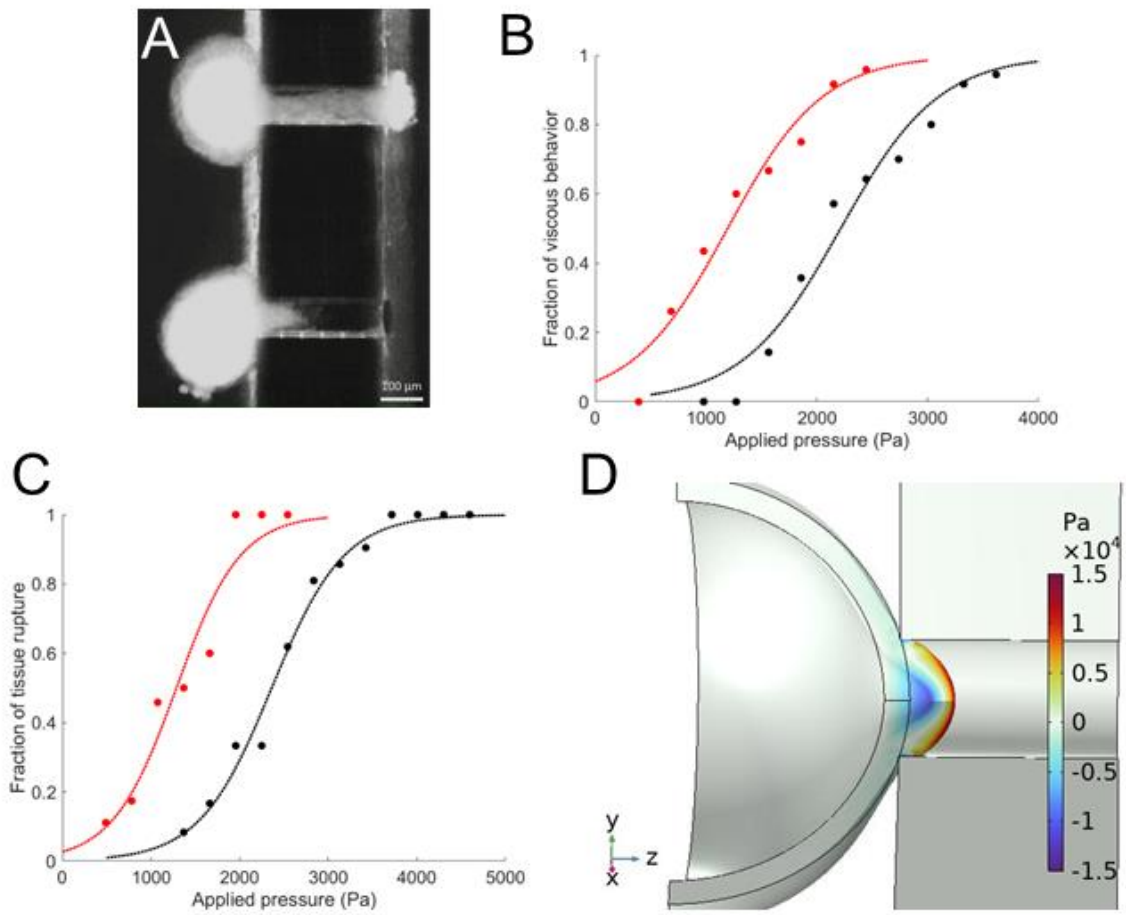

Fig 5. Critical stresses between different mechanical behaviors. A: snapshot of an experiment showing two similar samples displaying different behaviors at the same applied pressure. B: Quantification of the fraction of viscous behavior at different applied pressures. C: quantification of the fraction of samples showing tissue rupture as a function of applied pressure. In B

and C, dots are data and solid lines fit by a sigmoid function. In black are control samples and in red samples pretreated with 2mM EDTA. Each point is derived from 18 to 40 samples stemming from 8 different experiments in B and 4 in C. D: Numerical simulations. The color code represents the hoop stress within the aspirated shell when aspirated at the critical pressure 2.37kPa. Parameter values are the same as in Fig. 3.

The most naturel explanation for this lack of integrity is the weakening and rupture of cell-cell contacts since we often observed detachment of single cells, making a possible deadhesion of the tissues to the extracellular matrix unlikely. To verify this hypothesis, we repeated our measurement of the critical pressures required to induce either a viscous behavior or tissue rupture on tissue spheres pre-treated with 2mM EDTA. EDTA is a chemical well-known for weakening cell-cell adhesions in many epithelial tissues and we expected this treatment to facilitate the induction of a viscous behavior and tissue rupture. This is indeed what we found with a shift of the critical pressure from 2.22 kPa to 1.19 ± 0.16 kPa for the viscous behavior (Fig 5B) and from 2.37 kPa to 1.29 ± 0.19 kPa for rupture (Fig 5C).

It is important to note that all these measurements apply to the difference of pressure applied between the two sides of the holes and not necessarily to the stresses actually acting in the tissues themselves. Said differently, the applied pressure required to rupture the tissue shouldn't be directly taken as a measurement of the ultimate tensile stress of the whole tissue. To relate the applied pressure and internal tissue stresses, we turned again to numerical simulations. As described previously, we submitted a spherical shell with $R_0 = 170\ \mu m,\ h = 20\ \mu m,\ E = 11.4 \pm 8.3\ kPa,\ \nu = 0.4 - 0.49$ within a micropipette of radius $R_p = 50\mu m$ to an aspiration pressure of 2.37kPa, the critical pressure for rupture we measured experimentally. We then computed the hoop stress within the tunnel, averaged over the outer half of the shell on a thickness $h/2$ (Fig 5D). We measured a maximal average hoop stress to be in the range $7.4 \pm 0.5\ kPa$ where the error bars are obtained by varying the shell elastic modulus within the same range as above.

Since in normal conditions, the threshold for viscous behavior cannot be clearly distinguished from the threshold for rupture, our measurements revealed that up to rupture, which is also observed in normal osmotic oscillations, regenerating *Hydra* tissue spheres behave as linearly elastic spherical shells. This observation confirms experimentally an assumption often made in theoretical models of *Hydra* patterning (5,22). We will now expand these results to tissue mechanics during early *Hydra* regeneration.

Mechanical description of oscillating Hydra tissue spheres during regeneration.

After folding back into a spherical shape, regenerating *Hydra* tissue spheres experience a series of swelling-rupture cycles which have been shown to be driven by the difference in osmolarity between the inside and outside of the spheres. These oscillations and consecutive tissue rupture are required for the proper morphogenesis and regeneration of the samples although their exact role remains unknown. Thanks to previous work on the topic (5,40) and our own mechanical characterization, we can provide a good understanding of the internal tissue mechanics occurring during this phase.

Based on our experimental observations, we will approximate our samples as linearly elastic, symmetric, spherical shells of known, constant thickness, h and of varying radius $R(t)$ (Fig S5) submitted to a difference in osmolite concentrations $(C_{in} - C_{out}) > 0$. The spherical shells are submitted to two opposing pressures, the osmotic pressure $\Pi = (C_{in} - C_{out})RT$ where R is the ideal gaz constant and T is the temperature and a restoring elastic pressure due to the stretching of the sphere. Following the mechanics of spherical thin shells, this pressure can be written as:

$$P_{el} = \frac{4(R(t) - R_0)Eh}{2R_0^2(1-\nu)} \quad (8)$$

The fact that the spheres are constantly swelling indicates a constant influx of water into their lumen and that the system never reaches osmotic equilibrium. Furthermore, Kücken et al. (5) showed that the increase of $R(t)$ can be described by a Darcy-type law of the form:

$$\frac{dV}{dt} = 4\pi R(t)^2 L_w k_b T(C_{in} - C_{out}) \quad (9)$$

Where $V(t)$ is the volume of the sphere, L_w is the water permeability coefficient, k_b is Boltzmann's constant. In an oscillation cycle $R(t)$ increases up to a factor on the order of 1.2 (Fig S5) leading to an increase of the volume of the lumen by a factor of roughly 1.8. Dilution of the osmolite in the lumen should therefore be non-negligible and effectively slow down the swelling rate during an oscillation. To solve this discrepancy with experimental data, it is usually assumed that the tissue spheres expels waste into the lumen, effectively maintaining it at a constant concentration C_{in} leading to a constant osmotic imbalance. This imbalance can be estimated to be around 50mM as it is the necessary concentration of sucrose to add to the outside medium to completely stop the influx of water and the mechanical oscillations.

With this numerical value and our own mechanical characterization, we can estimate the equilibrium radius of a tissue sphere of rest radius $R_0 = 200\mu m$ at which the elastic restoring pressure balances the osmotic pressure and found it to be on the order of 2mm, an order of magnitude higher than the maximum radius actually reached experimentally. This calculation demonstrates that the oscillations occur as the system is far from osmotic equilibrium.

The dynamics of swelling is thus entirely controlled by the influx of water which imposes a constantly increasing deformation on the tissue sphere with a growth rate of the radius on the order of $5\mu m/h$ (Fig S5).

In order to understand the mechanics of the tissue and to study possible couplings with biochemical signals, one key quantity is the the circumferential or hoop stress which is given for an elastic spherical shell by, in the usual notations for spherical coordinates:

$$\sigma_{\varphi\varphi}(t) = \sigma_{\theta\theta}(t) = P_{el}\frac{R_0}{2h} \quad (10)$$

And which is known to control tissue integrity and to be able to alter key biological processes. Since $R_0 \gg h$, these stresses can be much larger than the elastic restoring pressure difference in the radial direction. In our case, we can include the value of P_{el} to find:

$$\sigma_{\theta\theta}(t) = \frac{E}{1-\nu}\frac{R(t) - R_0}{R_0} \quad (11)$$

the constitutive linear relationship between stresses and strains in the tissue during the oscillations which allows to directly extract the stress from a measurement of the size of the sample as a function of time.

Using these measurements of oscillations, the experimental measurement of E we previously obtained and the same estimate of the Poisson's ratio, $\nu = 0.49$, we were able to estimate these stresses during the oscillations and found them to be on the order of a few kPa (Fig S5). Most notably, this approach allowed us to estimate the critical stress, within the tissue, to induce rupture and we found it to be on the order of 4-5kPa, the same order of magnitude as obtained by aspiration experiments and numerical simulations.

Discussion

The effect of stretching on the biology of epithelial tissues has emerged in recent years as an important topic in developmental biology since developing organisms often undergo substantial deformations which have an increasingly recognized impact on their biological response. In the context of Hydra regeneration, Ferenc et al. observed that the levels of expression of Wnt ligands, especially HyWnt3, are directly linked to the cumulative amount of stretching in the tissue (17). In a similar fashion, stretching adhering monolayers of epithelial cells has been shown to induce cell division through the activation of Piezo1 mechanosensitive ion channels (19) to restore proper cell density. Anisotropic deformations also have a large impact on the tissue as uniaxial cyclic stretch leads to re-orientation of the cells perpendicular to the direction of application (41,42), as was observed for the mitotic spindle of single cells (43). In many of these experiments, however, stresses within the tissues couldn't be recorded after stretching.

One notable exception was achieved by seeding an epithelial monolayer on a stretchable hydrogel also embedded with tracers allowing to measure tension within the tissue (44). The authors found that upon stretch release after 10min elongation, the epithelial layer showed fracture, independent of the local tension. This might suggest that deformations, rather than stresses, might trigger rupture of the tissue. In *Hydra* osmotic oscillations, however, the two are coupled and could only be distinguished if one could modify the Young's modulus of the sample to decouple them. Another exception was achieved on freely suspended epithelia axially stretched with a measurable force (36). This experimental setup allowed the authors to estimate the Young's modulus of Madine–Darby Canine Kidney (MDCK) tissue to also be on the order of 20kPa. In addition, the authors found that the monolayer was able to withstand deformations up to 60% before rupturing, a value slightly higher than what is observed for *Hydra* tissue spheres.

In our case, the deformations of the tissues are isotropic and the three dimensional curved geometry of *Hydra* tissue spheres is different from flat monolayers. In addition, our mechanical description of the tissue spheres assumes a homogenous shell, ignoring the complex three layer (endoderm-extra-cellular matrix-ectoderm) structure of the samples. It is clearly possible that the deformations and stresses induced by the osmotic oscillations are differently transmitted and have different effects on these different layers, a refinement which will need to be addressed in the future. In particular, it was recently suggested that the mechanical properties of the ECM, which were not specifically measured here, could be linked to morphogenesis in *Hydra* (45).

One would like to be able to measure independently the value of the Poisson's ratio of *Hydra* tissue, a source of uncertainty in our estimates of rheological parameters. Another perspective opened by our work would be to calculate the response of a spherical viscoelastic shell to applied pressure, since this result could apply to many three dimensional tissues engulfing a lumen. Here, we used numerical simulations to estimate an unknown dimensionless factor in the elastic phase, while we ignored a similar pre-factor in the viscous regime.

Since we believe deformations and stresses within the tissues to be central in the morphogenesis of *Hydra*, another natural question is the existence of inhomogeneities of deformations, forces or rheological properties within the same sample. Mechanical fluctuations, if coupled to biochemistry, could well be sufficient to destabilize a reaction-diffusion system into a patterned state. Our own experimental setup could allow to measure fluctuations in rheological properties by repeating measurements on the same samples with small holes but at different locations, the main limitation being the lack of control of the position of the tested zone. In the same logic, it has been proposed that the amount of HyWnt3 protein could locally affect the Young's modulus of the tissue (22) which could couple the chemical patterning of the head organizer and morphogenesis. If the future location of the head becomes softer, the homogenous osmotic pressure will deform this region more, leading to a deviation from a spherical shape to an oblong one. Here too, our setup could allow to measure the Young's modulus of tissue spheres overexpressing HyWnt3 to directly test this hypothesis.

Conclusion

In this work, we have employed an original parallelized microaspiration device to characterize the mechanical behavior of *Hydra* tissue spheres. Although we found different rheological behaviors depending on the applied stresses, the main result we obtained is that during normal osmotic oscillations, these samples behave almost entirely as linearly elastic shells. Doing so, we also obtained quantitative measurements of their relevant rheological parameters ($E = 11.4 \pm 8.3\ \mathrm{kPa}$, $\eta = 2.4 \pm 1.2\ .\ 10^6\ \mathrm{Pa.s}$, critical applied pressures for viscous behavior and tissue rupture). This allowed us to estimate the stresses acting within the tissues and, in particular, the critical stress at which they start rupturing. These results, by allowing a quantification of both stresses and deformations during *Hydra* regeneration, will hopefully pave the way for quantitative approaches aiming at correlating these mechanical cues with molecular ones in order to understand *Hydra* patterning as an integrated mechano-biochemical process.

Author contributions

OCE designed the research. ZBM, MD and PJ manufactured the inserts. TP, ABB, PM and OCE performed the research and analyzed data. TP, PM and OCE wrote the manuscript which was reviewed by all authors.

Declaration of interests

The authors have declared no conflict of interest.

Acknowledgments

This work was funded by the Mission pour les Initiatives Transverses et Interdisciplinaires of CNRS (Project MeChemReg to OCE and PM). We thank H. Delanoë-Ayari for fruitful discussions.

References

1. Galliot B, Schmid V. Cnidarians as a model system for understanding evolution and regeneration. Vol. 46, International Journal of Developmental Biology. UPV/EHU Press; 2002.

675 p. 39–48.

676 2. Technau U, Steele RE. Evolutionary crossroads in developmental biology: Cnidaria.
677 Development. 2011 Apr;138(8):1447–58.

678 3. Gierer A, Berking S, Bode H, David CN, Flick K, Hansmann G, et al. Regeneration of hydra from
679 reaggregated cells. Nat New Biol. 1972 Sep 27;239(91):98–101.

680 4. Cochet-Escartin O, Locke TT, Shi WH, Steele RE, Collins E-MS. Physical Mechanisms Driving Cell
681 Sorting in Hydra. Biophys J. 2017 Dec 19;113(12):2827–41.

682 5. Kücken M, Soriano J, Pullarkat PA, Ott A, Nicola EM. An osmoregulatory basis for shape
683 oscillations in regenerating hydra. Biophys J. 2008 Jul;95(2):978–85.

684 6. Fütterer C, Colombo C, Jülicher F, Ott A. Morphogenetic oscillations during symmetry breaking
685 of regenerating Hydra vulgaris cells. Europhys Lett. 2003 Oct 1;64(1):137.

686 7. Broun M, Gee L, Reinhardt B, Bode HR. Formation of the head organizer in hydra involves the
687 canonical Wnt pathway. Development. 2005;132(12).

688 8. Bode HR. Axial Patterning in Hydra. Cold Spring Harb Perspect Biol. 2009;1(1).

689 9. Böttger A, Hassel M. Hydra, a model system to trace the emergence of boundaries in
690 developing eumetazoans. Int J Dev Biol. 2012;56(6–8):583–91.

691 10. Soriano J, Colombo C, Ott A. Hydra molecular network reaches criticality at the symmetry-
692 breaking axis-defining moment. Phys Rev Lett. 2006 Dec 18;97(25):258102.

693 11. Turing AM. The Chemical Basis of Morphogenesis. Philos Trans R Soc B Biol Sci. 1952 Aug
694 14;237(641):37–72.

695 12. Marcon L, Sharpe J. Turing patterns in development: What about the horse part? Curr Opin
696 Genet Dev. 2012 Dec;22(6):578–84.

697 13. Schweisguth F, Corson F. Self-Organization in Pattern Formation. Dev Cell. 2019 Jun
698 3;49(5):659–77.

699 14. Gierer A, Meinhardt H. A theory of biological pattern formation. Kybernetik. 1972
700 Dec;12(1):30–9.

701 15. Nakamura Y, Tsiairis CD, Özbek S, Holstein TW. Autoregulatory and repressive inputs localize
702 Hydra Wnt3 to the head organizer. Proc Natl Acad Sci U S A. 2011 May 31;108(22):9137–42.

703 16. Soriano J, Rüdiger S, Pullarkat P, Ott A. Mechanogenetic coupling of Hydra symmetry breaking
704 and driven Turing instability model. Biophys J. 2009 Feb 18;96(4):1649–60.

705 17. Ferenc J, Papasaikas P, Ferralli J, Nakamura Y, Smallwood S, Tsiairis CD. Mechanical
706 oscillations orchestrate axial patterning through Wnt activation in Hydra. Sci Adv. 2021 Dec
707 1;7(50):6897.

708 18. Desprat N, Supatto W, Pouille P-A, Beaurepaire E, Farge E. Tissue deformation modulates
709 twist expression to determine anterior midgut differentiation in Drosophila embryos. Dev Cell.
710 2008 Sep;15(3):470–7.

711 19. Gudipaty SA, Lindblom J, Loftus PD, Redd MJ, Edes K, Davey CF, et al. Mechanical stretch
712 triggers rapid epithelial cell division through Piezo1. Nature. 2017 Mar 15;543(7643):118–21.

713 20. Pouille P-A, Ahmadi P, Brunet A-C, Farge E. Mechanical signals trigger Myosin II redistribution
714 and mesoderm invagination in Drosophila embryos. Sci Signal. 2009 Apr 14;2(66):ra16.

715 21. Shinozuka T, Takada R, Yoshida S, Yonemura S, Takada S. Wnt produced by stretched roof-
716 plate cells is required for the promotion of cell proliferation around the central canal of the
717 spinal cord. Dev. 2019 Jan 15;146(2).

718 22. Mercker M, Köthe A, Marciniak-Czochra A. Mechanochemical symmetry breaking in Hydra
719 aggregates. Biophys J. 2015 May 5;108(9):2396–407.

720 23. Brinkmann F, Mercker M, Richter T, Marciniak-Czochra A. Post-Turing tissue pattern
721 formation: Advent of mechanochemistry. PLoS Comput Biol. 2018 Jul 1;14(7):e1006259.

722 24. Wang R, Goel T, Khazoyan K, Sabry Z, Quan HJ, Diamond PH, et al. Mouth Function
723 Determines the Shape Oscillation Pattern in Regenerating Hydra Tissue Spheres. Biophys J.
724 2019 Sep 17;117(6):1145–55.

725 25. Livshits A, Shani-Zerbib L, Maroudas-Sacks Y, Braun E, Keren K. Structural Inheritance of the
726 Actin Cytoskeletal Organization Determines the Body Axis in Regenerating Hydra. Cell Rep.
727 2017 Feb 7;18(6):1410–21.

728 26. Wang R, Steele RE, Collins EMS. Wnt signaling determines body axis polarity in regenerating
729 Hydra tissue fragments. Dev Biol. 2020 Nov 1;467(1–2):88–94.

730 27. Wang R, Bialas AL, Goel T, Collins E-MS. Mechano-Chemical Coupling in Hydra Regeneration
731 and Patterning. Integr Comp Biol. 2023 Jun 20;

732 28. Veschgini M, Gebert F, Khangai N, Ito H, Suzuki R, Holstein TW, et al. Tracking mechanical and
733 morphological dynamics of regenerating Hydra tissue fragments using a two fingered micro-
734 robotic hand. Appl Phys Lett. 2016 Mar 7;108(10).

735 29. Evans EA. New Membrane Concept Applied to the Analysis of Fluid Shear- and Micropipette-
736 Deformed Red Blood Cells. Biophys J. 1973 Sep 1;13(9):941–54.

737 30. Guevorkian K, Colbert M-J, Durth M, Dufour S, Brochard-Wyart F. Aspiration of Biological
738 Viscoelastic Drops. Phys Rev Lett. 2010;104(21):1–4.

739 31. Hochmuth RM. Micropipette aspiration of living cells. J Biomech. 2000 Jan;33(1):15–22.

740 32. Lim CT, Zhou EH, Quek ST. Mechanical models for living cells--a review. J Biomech.
741 2006;39(2):195–216.

742 33. Landiech S, Elias M, Lapèze P, Ajiyel H, Plancke M, Laborde A, et al. Parallel on-chip
743 micropipettes enabling quantitative multiplexed characterization of vesicle mechanics and cell
744 aggregates rheology. bioRxiv. 2023 Oct 22;2023.10.19.562871.

745 34. Boot RC, Roscani A, van Buren L, Maity S, Koenderink GH, Boukany PE. High-throughput
746 mechanophenotyping of multicellular spheroids using a microfluidic micropipette aspiration
747 chip. Lab Chip. 2023 Mar 3;23(7):1768.

748 35. Guevorkian K, Brochard-Wyart F, Gonzalez-Rodriguez D. Flow dynamics of 3D multicellular
749 systems into capillaries. In: Viscoelasticity and Collective Cell Migration: An Interdisciplinary
750 Perspective Across Levels of Organization. Academic Press; 2021. p. 193–223.

751 36. Harris AR, Peter L, Bellis J, Baum B, Kabla AJ, Charras GT. Characterizing the mechanics of
752 cultured cell monolayers. Proc Natl Acad Sci U S A. 2012 Oct 9;109(41):16449–54.

753 37. Ugural AC. Stresses in beams, plates, and shells, third edition. CRC Press; 2009. 576 p.

754 38. Sato M, Theret DP, Wheeler LT, Ohshima N, Nerem RM. Application of the Micropipette
755 Technique to the Measurement of Cultured Porcine Aortic Endothelial Cell Viscoelastic
756 Properties. J Biomech Eng. 1990 Aug 1;112(3):263–8.

757 39. Tsai MA, Frank RS, Waugh RE. Passive mechanical behavior of human neutrophils: power-law
758 fluid. Biophys J. 1993 Nov 1;65(5):2078–88.

759 40. Ruiz-Herrero T, Alessandri K, Gurchenkov B V., Nassoy P, Mahadevan L. Organ size control via
760 hydraulically gated oscillations. Development. 2017 Dec 1;144(23):4422–7.

761 41. Lien JC, Wang Y li. Cyclic stretching-induced epithelial cell reorientation is driven by
762 microtubule-modulated transverse extension during the relaxation phase. Sci Reports 2021
763 111. 2021 Jul 20;11(1):1–12.

764 42. Gérémie L, Ilker E, Bernheim-Dennery M, Cavaniol C, Viovy JL, Vignjevic DM, et al. Evolution of
765 a confluent gut epithelium under on-chip cyclic stretching. Phys Rev Res. 2022 Jun
766 1;4(2):023032.

767 43. Fink J, Carpi N, Betz T, Bétard A, Chebah M, Azioune A, et al. External forces control mitotic
768 spindle positioning. Nat Cell Biol 2011 137. 2011 Jun 12;13(7):771–8.

769 44. Casares L, Vincent R, Zalvidea D, Campillo N, Navajas D, Arroyo M, et al. Hydraulic fracture
770 during epithelial stretching. 2015;

771 45. Veschgini M, Suzuki R, Kling S, Petersen HO, Bergheim BG, Abuillan W, et al. Wnt/β-catenin
772 signaling induces axial elasticity patterns of Hydra extracellular matrix. iScience. 2023 Apr
773 21;26(4):106416.

774

775 **Supplemental movie legends**

776

777 Movie S1. Timelapse of sample loading for microaspiration experiments in a 6-opening insert.

778

779 Movie S2. Example of tissue rupture in a 100μm-wide square opening for an applied pressure of
780 3kPa. Endoderm is shown in magenta and ectoderm in green.

781

782 Movie S3. Long term elastic behavior of six Hydra tissue spheres. Endoderm is shown in magenta and
783 ectoderm in green.